Competition between heterogeneous and homogeneous nucleation near a flat wall

2009 J. Phys.: Condens. Matter 21 464115

(http://iopscience.iop.org/0953-8984/21/46/464115)

J. Phys.: Condens. Matter **21** (2009) 464115 (10pp) doi:10.1088/0953-8984/21/46/464115

Competition between heterogeneous and homogeneous nucleation near a flat wall

Patrick Wette[1,4], Andreas Engelbrecht[2], Roushdey Salh[2], Ina Klassen[1], Dirk Menke[1], Dieter M Herlach[1], Stephan V Roth[3] and Hans Joachim Schöpe[2,4]

[1] Institut für Materialphysik im Weltraum, Deutsches Zentrum für Luft- und Raumfahrt (DLR), D-51170 Köln, Germany
[2] Institut für Physik, Johannes Gutenberg-Universität, Staudinger Weg 7, D-55128 Mainz, Germany
[3] HASYLAB, DESY, Notkestrasse 85, D-22603 Hamburg, Germany

Received 22 April 2009, in final form 17 June 2009
Published 27 October 2009
Online at stacks.iop.org/JPhysCM/21/464115

Abstract
We studied the competition between heterogeneous and homogeneous nucleation of an aqueous suspension of charged colloidal spheres close to the container walls. Samples of equilibrium crystalline structure were shear-melted and the metastable melt left to solidify after the cessation of shear. The crystallization kinetics was monitored using time-resolved scattering techniques: at low particle number densities n we applied an improved static light scattering method while at large particle concentrations ultra-small-angle x-ray scattering was applied for the first time. Our results show some unexpected behavior: the heterogeneous nucleation at the container walls is delayed in comparison to the homogeneous bulk nucleation and its rate density appears surprisingly slightly smaller, demonstrating the complexity of the observed crystallization process.

(Some figures in this article are in colour only in the electronic version)

1. Introduction

Understanding the process that drives an undercooled fluid to the crystal state is still a challenging issue for condensed matter physics. One promising approach to the problem is offered by the study of colloidal suspensions, which can be regarded as 'macroatoms'. These offer, compared to true atomic systems, a number of advantages. On one side, the interaction potential in colloidal macroatoms can be finely controlled and tuned by the experimentalists, by engineering the properties of the particles and/or changing the characteristics of the dispersing medium. On the other side, typical length and timescales of colloidal systems shifted by orders of magnitude as compared to atomic systems allowing for direct, time-dependent studies of the solidification process with easily manageable experimental techniques such as microscopy, light scattering or even x-ray scattering. Throughout the past few years the problem of solidification of the melt via homogeneous and heterogeneous nucleation has been addressed in colloidal systems mainly of monodisperse colloidal spheres suspended in a fluid.

For colloidal systems there exist numerous computer simulations and numerical calculations on homogeneous nucleation particularly for hard-sphere systems due to their easy-to-use interaction potential [1–3]. On the experimental side extensive crystallization experiments have been performed on systems of hard-sphere colloids using time-resolved laser light scattering or microscopy [4–8]. Meanwhile the focus has also shifted to solidification of colloidal systems of different interactions [9]. In particular, the nucleation kinetics of charged systems, interacting via screened Coulomb potentials, has been investigated in some studies. Therefore charged systems are the second class of colloids, where systematic experiments on their solidification from the undercooled melt have been reported [10–14].

A little is known about the influence of potent substrates on the kinetics of the crystallization from the melt. Meanwhile there exists some experimental as well as theoretical studies dealing with unstructured and structured substrates [15–18]. At unstructured substrates both hard-sphere and charged-sphere crystals wet with their densest packing plane ((111) for fcc and (110) for bcc) forming oriented nuclei, which further may

[4] These authors contributed equally to this work.

be aligned using external shearing fields [19, 20]. Depending on the interaction conditions planar growth fronts or columnar growth may result [21]. Also more complex situations of heterogeneous phase formation have been investigated so far. Recently heterogeneous nucleation events on curved surfaces or on spherical impurities in the colloidal melt have been examined in experiments [22] as well as in computer simulations [23]. Multiple nucleation sites were observed for large spherical impurities as well as the frustration of nucleation at smaller ones.

As revealed by experiment, theory and simulation, both equilibrium phase behavior and solidification kinetics in the presence of confining walls and formerly applied shear differ considerably from bulk situations. Shear has turned out to be one of the most versatile tools to extend nucleation control on flat unstructured walls through the possibility of forming metastable shear-induced structures under flow. These may in principle determine the structure of the nuclei and thus the morphology and orientation of the final crystal. Stipp *et al* presented recently an extensive experimental study on the influence of shear on heterogeneous nucleation on flat unstructured walls of highly charged spheres dispersed in low salt or deionized water during and after the cessation of shear [24]. At low particle number densities near the fluid–solid phase boundary they observed that shear would lead to the formation of layer structures. Upon cessation of shear large single crystallites of the preferred structure occur through the registering of layers. The lateral growing crystals obey a classical Wilson–Frenkel law.

Especially in non-sedimenting charged-sphere systems at elevated particle number density homogeneous bulk nucleation may also occur and the solidification process near the wall becomes more complex [24, 25]. The homogeneous nucleation increases in volume as the interaction is increased. Wall nucleation is then terminated by intersection with the bulk crystalline material. This hinders it to observe pure heterogeneous nucleation without special precautions especially when the metastability is larger and the solidification process becomes dominated by homogeneous nucleation events and subsequent growth of the nuclei. In these situations, where a competition between homogeneous and heterogeneous nucleation occurs, time-resolved experimental observation methods are highly desirable, which have the capability to distinguish between the two appearing nucleation processes and simultaneously observe the phase formation from its initial states to the complete solidified sample with regard to homogeneous and heterogeneous induced solidification.

In this contribution we present extended time-resolved scattering methods which enable the distinction between heterogeneous and homogeneous nucleation and a quantitative access to these competing solidification processes close to a flat wall for the very first time. The first technique to be employed is an extended light scattering method where a larger scattering vector range is observed with a linear CCD array at once, similar to former applied techniques [26, 27]. By means of a skillful arrangement of the aperture setting we are able to exclude the scattering signal of either wall-based heterogeneous nucleation or homogeneous nucleation occurring in the center of the cell. This method is applicable at lower particle number densities where sample turbidity is low and multiple scattering events can be excluded. At elevated particle number densities we applied the ultra-small-angle x-ray-scattering (USAXS) technique. Here a novel high speed detector was employed allowing for time-resolved detection of 2d scattering patterns. This has the advantage that appearing heterogeneous nucleated wall crystals can be distinguished from homogeneous bulk material due to there appearing sixfold symmetric scattering patterns superimposed on a continuous scattering pattern ascribed to homogeneous bulk nucleation.

This paper is organized as follows. We start with an introduction of the chosen charged-sphere suspensions and their conditioning. The two experimental observation techniques are presented in detail, followed by a presentation of the first results highlighting the competition between homogeneous and heterogeneous nucleation. We shall close with a short discussion of the observed nucleation scenarios.

2. Systems and system preparation

2.1. Charged-sphere suspensions

The study presented here focuses on crystallizing charged-sphere suspensions, where the particles carry acidic end group molecules on their surfaces which start to dissociate in a deionized suspension medium like water or organic solvents, leaving a population of spheres having equal negative charges with narrow limits. The spheres and their associated counterion distribution interact via repulsive electrostatic forces, which can be modeled by a Debye–Hückel potential:

$$V(r) = \frac{(Z^*e)^2}{4\pi\varepsilon\varepsilon_0}\left(\frac{\exp(\kappa a)}{1+\kappa a}\right)^2\frac{\exp(-\kappa r)}{r} \qquad (1a)$$

with

$$\kappa^2 = \frac{e^2}{\varepsilon\varepsilon_0 k_B T}(nZ^* + c_{s,b}), \qquad (1b)$$

where a is the particle radius, $\varepsilon\varepsilon_0$ is the dielectric permittivity and k_BT is the thermal energy. The screening parameter κ contains the contributions of particle counterions nZ^*, excess salt or base molar concentration $c_{s,b}$. Particle number density can be obtained via static light scattering, while Z^* can be obtained either from measurements of the elasticity in polycrystalline samples [28] or from measurements of the conductivity [29].

Crystals form spontaneously in charged-sphere systems of low electrolyte concentration when the particle number density n exceeds a critical value which typically is of the order of 0.1–1 μm^{-3}. This corresponds to packing fractions $\Phi = n4/3\pi a^3$ as low as 10^{-4}–10^{-2}, where a is the particle radius. On the other hand, crystallization can also be induced by increasing the surface charge density by controlling the degree of dissociation of the acidic end groups. Typical particle distances then are of the order of the wavelength of visible light. The large center–center distance has the consequence that such crystals are extremely soft and fragile objects with shear moduli in the Pascal range. They can be shear-melted

Table 1. Compilation of the particle system properties. Particle system name; nominal diameter $2a$; polydispersity determined via ultracentrifugation (UZ) and/or scattering data via Mie theory (Mie); effective charges Z_G^* and Z_σ^* from shear modulus and conductivity measurements; the bare-particle charge as determined by conductometric titration. The last column gives the investigated particle number density range.

Particle system	Diameter $2a$ (nm)	Polydispersity (%)	Z_G^*	Z_σ^*	Particle surface charge (bare charge)	Investigated particle range n (μm^{-3})
Si86	86	8 (Mie)	255 ± 14–342 ± 20	381 ± 34–470 ± 30	4550 ± 160	18–110
PnBAPS122	122	2 (UZ)	582 ± 18	743 ± 40	n/a	0.5–5

by the slightest mechanical perturbation and then the re-crystallization can be observed via either optical methods or x-rays.

2.2. Chosen particle suspension

The colloidal dispersions used have to fulfill several requirements. First, of course, they have to show crystallization at all. Therefore particle samples of narrow size distribution were used. For light scattering an industrial batch of poly-n-butylacrylamide copolymer particles (a kind gift of BASF) and for USAXS investigations home-made silica (SiO_2) particles have been employed (Lab codes PnBAPSXX and SiXX, where XX denotes the diameter in nm). All properties of the chosen particle systems are summarized in table 1.

The PnBAPS122 particle system shows a size distribution of 2%. The range of observed crystallization extends down to $n = 0.5\ \mu\text{m}^{-3}$ ($\Phi = 0.000\,35$), leading to particle distances up to $d \approx 2\ \mu$m. The large particle distance at low particle number densities makes this system highly appropriate for light scattering and microscopic experiments, but the large scattering contrast restricts the range of concentrations for optically transparent samples to some $5\ \mu\text{m}^{-3}$. Above, multiple scattering effects occur and interfere with static and dynamic light scattering. The large particle distances and the low scattering contrast with regard to x-ray scattering makes the application of USAXS more difficult. Due to this, investigations are restricted to optical methods at low particle number density.

Investigations of the structure and the phase transition kinetics at larger particle number density USAXS studies can be enabled with silica systems due to the high electron contrast of the particles in an aqueous environment. The here employed Si86 particle system shows a somewhat larger size distribution of 8% and the particle concentration of the stock suspension was increased to $n = 110\ \mu\text{m}^{-3}$ ($\Phi = 0.035$). Crystallization can be observed down to a particle number density of $n \approx 18\ \mu\text{m}^{-3}$ ($\Phi = 0.0067$), leading to mean particle distances between 270 and 500 nm. The system is also accessible to light scattering and microscopy but, due to shorter particle distances, this system is also highly appropriate for USAXS investigations.

2.3. Interaction control and sample conditioning

The adjustment of the interaction strength of the polystyrene particles can be controlled via the particle number densities and via the amount of screening electrolyte. Increasing n and reducing the excess electrolyte concentration $c_{s,b}$ leads to higher interaction potentials as referred to from equations (1). Silica particles behave more complex. These particles carry weakly acidic silanol groups (Si–OH). Different to particles with stronger acidic end groups the degree of dissociation of the silanol end groups and therefore the surface charge may be increased by the addition of sodium hydroxide following the reaction: $\text{SiOH} + \text{NaOH} \rightarrow \text{SiO}^- + \text{Na}^+ + \text{H}_2\text{O}$, until all surface groups are dissociated, corresponding to a maximum effective interaction. Further addition of NaOH then leads to a screening effect, which subsequently reduces the interaction between the particles. For aqueous silica dispersions, the particle number density n and the NaOH concentration c_{NaOH} are the control parameters for the screened Coulomb interaction [30]. Both particle species were inspected in dependence on n and $c_{s,b}$ and fluid–solid phase boundaries were determined, resulting in a full description of the phase behavior. Deviations from equilibrium are described by the chemical potential difference, $\Delta\mu$, between the metastable and stable fluid and were determined via growth measurements following the method of Würth [13, 31]. It was also determined that both suspensions crystallize in a bcc structure over the entire investigated interaction range.

The samples are conditioned in a computer-controlled closed Teflon®-tubing system for controlling the interactions in the colloidal particle systems. The tubing connects different components. These comprise a mixed-bed ion exchange column, a reservoir to add solvent or salt solution, the sample cell (for microscopy, light scattering or USAXS measurement) and a conductivity experiment to control the particle number density n for deionized suspensions and/or the salt or sodium hydroxide concentration $c_{\text{salt,NaOH}}$. The suspension is driven through the preparation circuit by a peristaltic pump under an inert argon atmosphere to avoid contamination with airborne CO_2 [29]. Both solvent and electrolyte are added using a computer-controlled dosimeter (Titronic Universal, Schott AG, Germany). Computer-controlled electromagnetic valves stop the flow instantaneously. This marks the start of a crystallization experiment and ensures that the relaxation into the equilibrium state occurs without any (external) forces.

3. Experimental details

3.1. Time-resolved static light scattering

To investigate the crystallization kinetics in colloidal charged spheres with lower particle concentration we used time-resolved static light scattering. For this purpose we optimized

the illumination and detection optics of a home-built laser light scattering goniometer [32] and installed a linear CCD detector (LARRY-USB 2048, Ames Photonics). We use a special cell of cylindrical cross section (10 mm in diameter) which can be connected to our continuous conditioning system adjusting and controlling the interaction parameters carefully. For illumination a broad, parallel beam is required, to ensure good powder averaging. Using a beam expander in combination with a rectangular aperture a beam of rectangular cross section (4 mm in width and 25 mm in height) is realized. Using two cylindrical lenses the scattered light is focused on the linear CCD detector mounted on the goniometer arm leading to a simultaneously detected scattering range of 20°, an angle resolution of 0.01° and a time resolution of 38 ms. To study the crystallization kinetics of homogeneous nucleated crystals and heterogeneous nucleated wall crystals we modified the detection optics introducing special apertures giving us the possibility to measure the crystallization kinetics in the whole sample cell, solely in the center or only close to the wall (see figure 1). The data acquisition is performed using a self-written LabView® program controlling the detector, the goniometer stage and the sample conditioning system, allowing automated measurements. We averaged over 50 measurements to obtain meaningful data especially at short times. This set-up gives us the possibility to determine the fast crystallization kinetics in colloidal charged-sphere suspensions with excellent statistics, and angular and time resolution.

Figure 2 shows the time evolution of the crystal structure factor of the PnBAPS122 sample at $n = 1.15\ \mu\text{m}^{-3}$ and $c_s = 0.1\ \mu\text{M}$ (corresponding to a chemical potential difference of $\Delta\mu = 4k_BT$) for three sample volumes: (a) in the whole sample cell, (b) solely in the center and (c) only close to the wall. Detecting the scattered intensities of the complete scattering volume illuminated by the laser beam we observe a broad peak at short times. At intermediate times the peak becomes asymmetric and at late times two clear peaks can be observed. The broad peak is stemming from a homogeneous nucleated crystal, while the sharp one is caused by heterogeneous nucleated wall crystals. Unfortunately it is impossible to separate both signals at early times. At late times a fit of two Gaussian peaks can be performed. The crystallization kinetics of homogeneous nucleated crystals can be determined detecting the scattering signal stemming from the sample center. Here a single peak can be observed growing in intensity which can be well described by a Gaussian.

Observing a scattering volume close to the wall of the sample cell we again detect a signal originated by the wall crystals and by homogeneous nucleated crystals. As the scattered intensity stemming from both types of crystals is of the same value at early times, we are able to determine the competition between homogeneous and heterogeneous crystallization close to the wall by fitting two Gaussians to the structure factor.

From these measurements the time trace of the absolute crystallinity $X(t)$, the average crystal size $L(t)$, the number density of crystallites $n_{\text{xtal}}(t)$ and the nucleation rate density J can be determined.

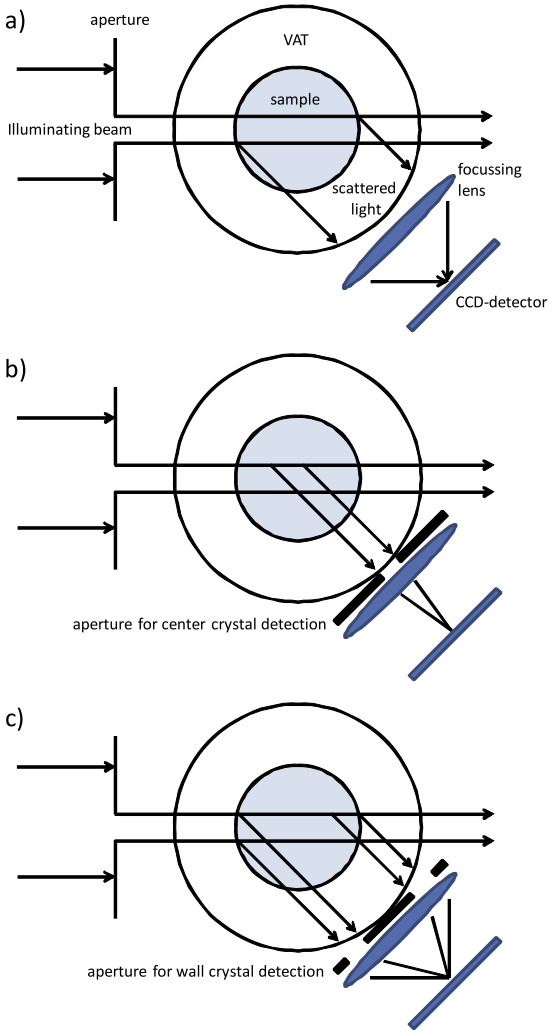

Figure 1. Different detection schemes determining the crystallization kinetics. The sample cell is illuminated with a broad parallel beam. The scattered light is focused with cylindrical lenses on a linear CCD array covering a scattering angle range of 20°. The setting of the aperture between the sample and detection optics enables a selection of the scattered intensity emitted from different positions in the sample cell: (a) of the whole sample cell, (b) solely in the center and (c) only close to the wall.

3.2. Time-resolved USAXS

We carried out the measurement at the soft matter beamline (BW4) at HASYLAB Hamburg. The BW4 at HASYLAB is a wiggler beamline with instrumentation to measure small-angle x-ray and ultra-small-angle x-ray scattering and supposed as a high flux material research set-up. The x-radiation coming from the wiggler is monochromized by means of a double-crystal monochromator and is focused onto the detector by means of a horizontal and vertical mounted mirror and has a standard wavelength of $\lambda = 0.138$ nm [33]. A second prototype of a new detector type was employed for the first time to investigate the fast crystallization kinetics of charged-sphere systems. The PILATUS100K two-dimensional detector [34] has an active area of $84 \times 34\ \text{mm}^2$ with pixel sizes of $172 \times 172\ \mu\text{m}^2$. PILATUS detectors feature several advantages compared to current state-of-the-art CCD and

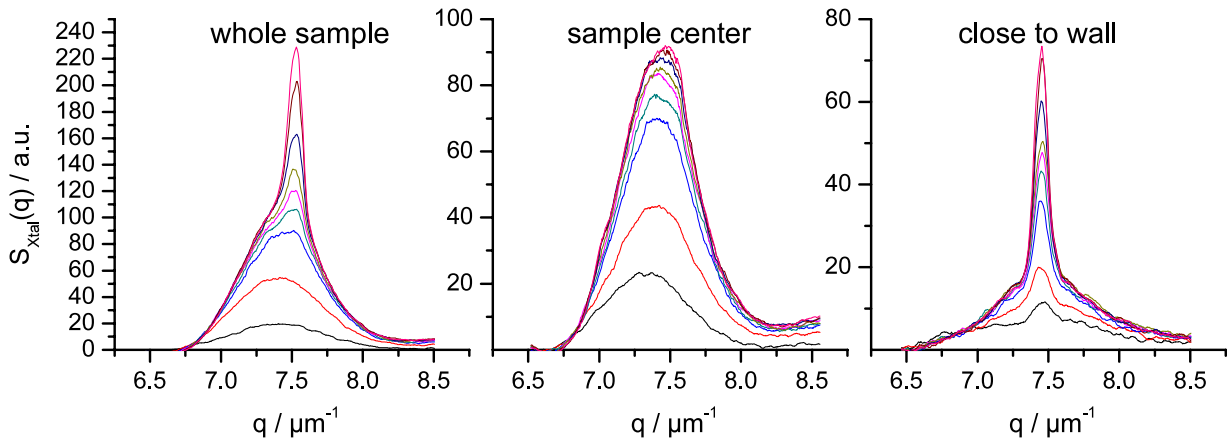

Figure 2. Time evolution of the crystal structure factor (bcc 110 peak) in different observed sample volumes shown for the PnBAPS122 sample at a particle number density of $n = 1.15\ \mu\text{m}^{-3}$ and a salt concentration of $c_s = 0.1\ \mu\text{M}$ ($\Delta\mu = 4k_BT$). The left plot shows the scattered intensity of the whole sample cell corresponding to the detection scheme in figure 1(a), while the middle and the right plot the partitioned structure factor corresponding to the schemes in figures 1(b) and (c), respectively.

imaging plate detectors. The main features include: high frame rate up to 100 Hz and short readout times of 5 ms, no readout noise, superior signal-to-noise ratio and high detected quantum efficiency. This ensures a good picture quality even at short illumination periods. The sample–detector distance can be varied between 1 and 13 m. Due to expected mean particle distances between 270 and 500 nm of the Si86 system a sample–detector distance of up to 13 m is necessary to ensure a sufficient resolution. The exact distance was determined with a collagen sample to be 13.4 m. The scattered intensity was measured in dependence on the scattering vector as well as on the particle form factor $P(q)$. With the x-ray intensity I_0 measured with a standard lupolen sample the formula $I(q) = I_0 P(q) S(q)$ can be used to calculate the structure factor $S(q)$.

A suitable sample cell was used to realize the measurements in which the colloidal dispersions can be controlled during the USAXS measurements. The cell has suitable connections for the computer-controlled preparation circuit used. A thin Kapton® film with a thickness of 25 μm was used as window material which ensures good transmission at a wavelength of $\lambda = 0.138$ nm used in the present experiments. The windows diameter is 4 mm. The sample volume is about 100 mm^3 and the wall-to-wall distance is 2 mm.

The detector time resolution was chosen to be 0.25 s with a readout time of 5 ms. A measurement sequence at adjusted particle number density and NaOH-concentration of 80 pictures is taken within 20 s. We carefully checked that the particle charge was not altered by exposure to x-rays. The pre-evaluation of the diffraction pattern includes normalization of the scattered intensities, background and the transmission correction and follows a standard procedure which is described in detail elsewhere [35].

A typical background and transmission corrected picture sequence of the Si86 system at $n = 71\ \mu\text{m}^{-3}$ and $c_{\text{NaOH}} = 1.5\ \text{mmol}\,\text{l}^{-1}$ (corresponding to a chemical potential difference of $\Delta\mu = 0.85 k_BT$) close to the fluid–solid phase boundary is shown in figure 3. The inner Debye–Scherrer ring first increases its intensity homogeneously. This can be ascribed to the appearance of a polycrystalline material. After approximately 2 s a sixfold pattern growth out of the inner ring increases to its maximum intensity after about 8.0 s. This pattern can be ascribed to the nucleation and growth of a wall-based twinned bcc crystal with its (110) plane parallel to the cell wall. Further details of structural identification of 2d scattering patterns of charged stabilized colloidal dispersions are given elsewhere [36–38].

This picture sequence shows one of the main advantages of the USAXS method: with the scattering information we can discriminate polycrystalline material from oriented wall-based crystals. The scattering pattern of these wall-based crystals can be identified by its sixfold symmetry while the scattering pattern of the polycrystalline material in the cell middle results in a full Debye–Scherrer ring.

To determine the crystallization kinetics of heterogeneous and homogeneous nucleated crystals the scattering signal of these two kinds of crystals had to be separated. This was done by masking out the respective sectors in the 2d scattering pattern followed by an azimuthal averaging of the remained scattering pattern as shown in figure 4. Finally the azimuthal integration of the first Debye–Scherrer ring with regard to the heterogeneous nucleation was corrected by subtracting the still underlying homogeneous contributions.

3.3. Data analysis

To determine the crystallization kinetics using time-resolved static scattering techniques we followed the data analysis proposed by Harland and van Megen [39]. The samples were shear-melted pumping the suspension through the sample cell as described above. The first scattering pattern is recorded directly after stopping the pumping process. We set this as the time $t = 0$ when, we assume, the system is still in the metastable fluid state. The subsequent emerging of the crystal phase is monitored with a time resolution of up to 38 ms (SLS) and 250 ms (USAXS), and characterized by the scattering

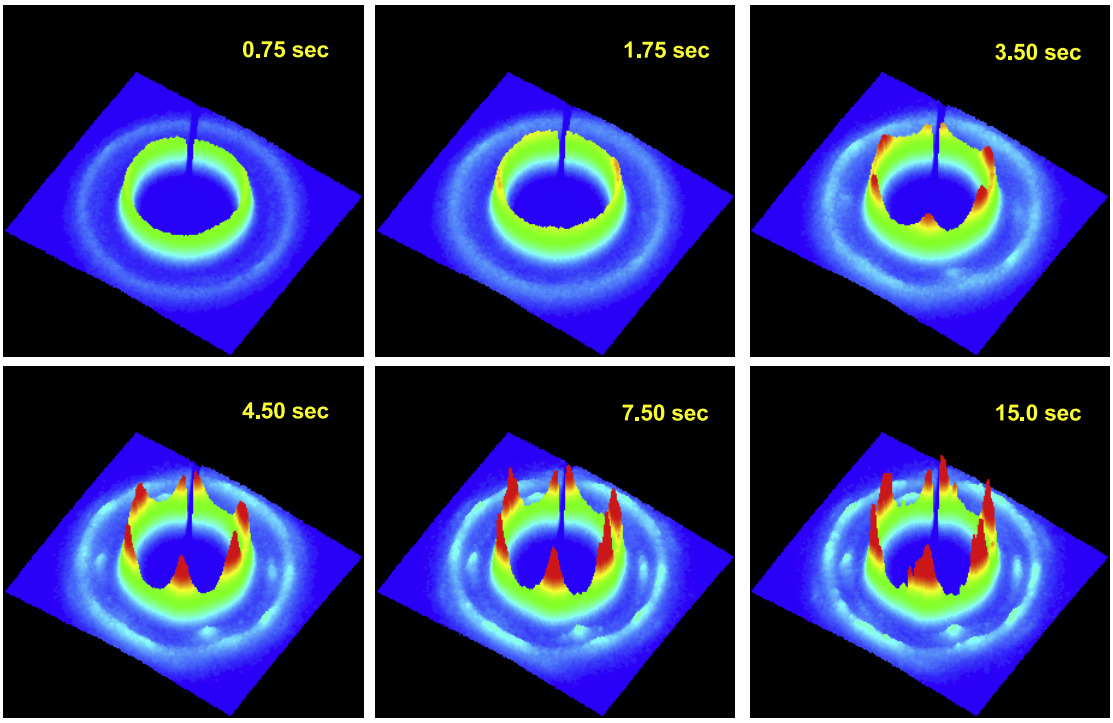

Figure 3. Three-dimensional transmission and background-corrected USAXS sequence of the Si86 particle system at $n = 71\ \mu\text{m}^{-3}$ and $c_{\text{NaOH}} = 1.5$ mmol l^{-1} ($\Delta\mu = 0.85 k_{\text{B}}T$) very close to the fluid–solid phase transition. x and y axes describe the pixel coordinates of the detector area and the z direction represents the intensity. The intensity of the inner Debye–Scherrer ring first increases homogeneously. After about 2 s a sixfold pattern growth out of the inner ring increases to its maximum intensity after about 8.0 s. In the same time the homogeneous part of the inner ring reduces its intensity.

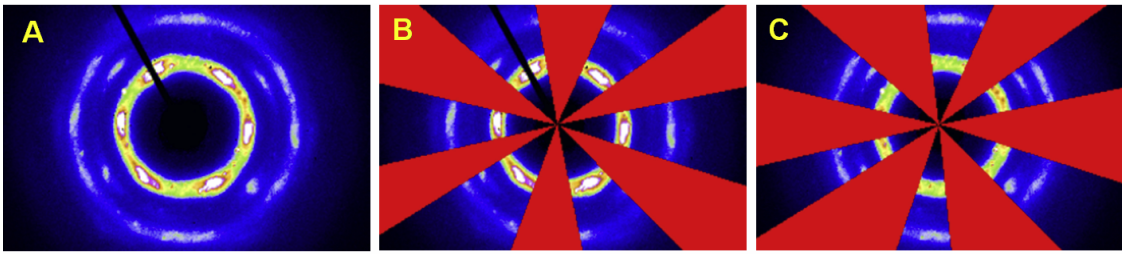

Figure 4. (A) Transmission and background-corrected 2d USAXS pattern of the Si86 suspension at $n = 71\ \mu\text{m}^{-3}$ and $c_{\text{NaOH}} = 1.25$ mmol l^{-1} ($\Delta\mu = 0.85 k_{\text{B}}T$), showing a sixfold symmetry in the first Debye–Scherrer ring. The picture was taken after complete solidification at $t = 20$ s. The thick black line cutting through the whole scattering pattern from the top left to the middle is due to the beam stop holder. It is excluded from the whole evaluation procedure. (B) Same diffraction pattern as shown in (A) but with an applied mask to exclude the sectors of the first Debye–Scherrer ring not contributing to the sixfold scattering pattern regarding heterogeneous nucleation. (C) The same situation as in (B), but here the inverse of the mask in (B) was applied to catch the contributions of the inner Debye–Scherrer cone regarding homogeneous nucleation.

intensity from the crystal:

$$I_{\text{xtal}}(q,t) = I(q,t) - \beta(t) I_{\text{fluid}}(q). \tag{2}$$

The time evolution of single Bragg peaks is analyzed by performing a best fit with a Gauss function. From the fitting parameters $A(t)$ (integrated area of the peak), $\delta q(t)$ (full width at half-maximum of the peak) and q_{hkl} (position of the peak) the following information can be obtained.

(1) The crystallinity $X(t)$ (the fraction of the sample which is crystalline) is calculated from the peak area:

$$X(t) = cA(t), \tag{3}$$

where c is a normalization factor based on the equilibrium phase diagram;

(2) The average linear dimension of the crystallites $L(t)$ is calculated from the full width at half-height of the peak $\delta q(t)$:

$$\langle L(t) \rangle = \frac{2\pi K}{\delta\, q(t)}, \tag{4}$$

where K is the Scherrer constant;

(3) The lattice constant g of the crystal phase is calculated from the peak position q_{hkl}:

$$g(t) = \frac{2\pi}{q_{hkl}(t)} \sqrt{h^2 + k^2 + l^2}, \tag{5}$$

where h, k, l are the Miller indices.

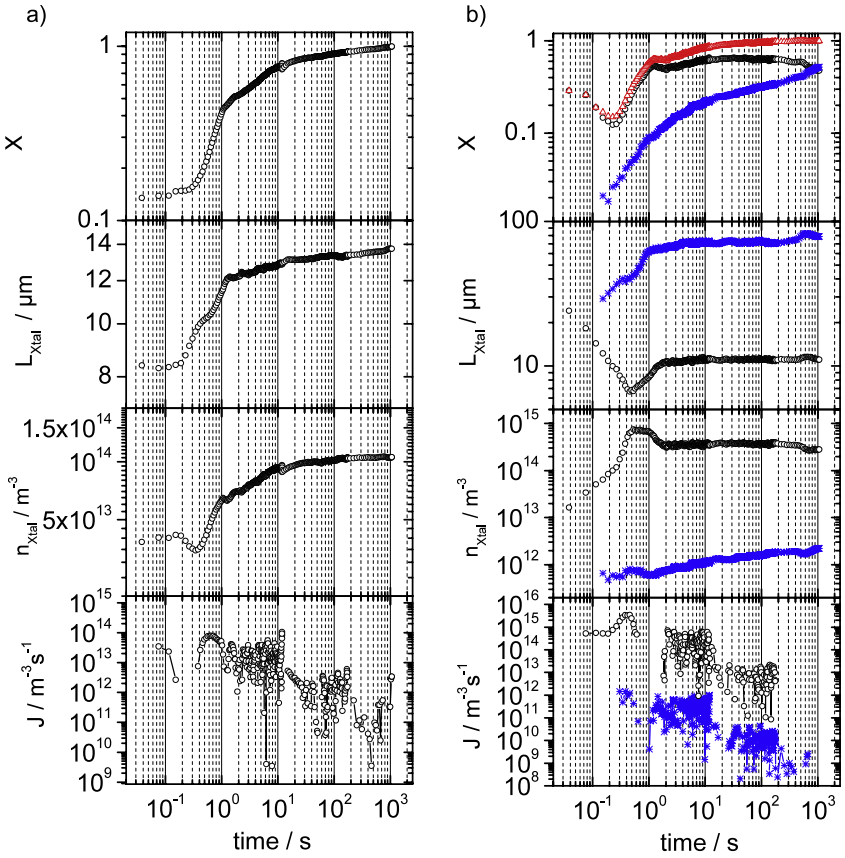

Figure 5. Time traces of the crystallization kinetics of the crystallinity X, the average crystal size L_{xtal}, the crystallite number density n_{xtal} and the nucleation rate density J of center crystals (a) and wall crystals (b) of the PnBAPS122 sample at $n = 1.15\ \mu\mathrm{m}^{-3}$, $c_{\mathrm{s}} = 0.1\ \mu\mathrm{M}$ ($\Delta\mu = 4k_{\mathrm{B}}T$) as determined via time-resolved static light scattering. The black open circles show the results for homogeneous and the blue colored stars for heterogeneous nucleation. The red open squares in the right plot denote the overall crystallinity close to the wall. The nucleation rate density is given by a five-point smoothing.

From these basic parameters, the following quantities can be determined.

(4) The number density of homogeneous nucleated crystallites

$$n_{\mathrm{xtal}}^{\mathrm{hom}}(t) = \frac{X_{\mathrm{hom}}(t)}{\langle L_{\mathrm{hom}}^3(t)\rangle} \approx \frac{X_{\mathrm{hom}}(t)}{\langle L_{\mathrm{hom}}(t)\rangle^3} \tag{6}$$

and wall-nucleated crystals

$$n_{\mathrm{xtal}}^{\mathrm{wall}}(t) = \frac{X_{\mathrm{wall}}(t)}{\langle L_{\mathrm{wall}}(t_{\mathrm{start}})\rangle \langle L_{\mathrm{wall}}^2(t)\rangle}, \tag{7}$$

where $\langle L_{\mathrm{wall}}(t_{\mathrm{start}})\rangle$ denotes the averaged crystal size at the start of the crystallization process. Using this expression we assume that heterogeneous nucleated wall crystals appear in a volume defined by the container wall area and the crystal size is determined in the first non-fluid scan.

(5) The nucleation rate density for homogeneous and heterogeneous nucleation, defined as the rate at which crystallites appear in the liquid volume:

$$J(t) = \frac{1}{1 - X(t)} \frac{\mathrm{d}}{\mathrm{d}t} n_{\mathrm{xtal}}(t). \tag{8}$$

4. Results and discussion

In the following we will present the first results discovering the competition between heterogeneous and homogeneous nucleation close to a flat wall. Using high precision time-resolved scattering methods we obtain the time trace of the crystallization scenario including heterogeneous and homogeneous nucleation and the microstructure evolution afterward. Our measurements allow a quantitative description of the competing processes highlighting the complexity of the solidification process in the presence of container walls.

4.1. Light scattering data

In figure 5(a) we present the crystallization kinetics of homogeneous nucleated crystals in the sample cell center. The observed crystallization scenario is in good agreement with previous investigations done in colloidal hard spheres [40].

The crystallinity first increases slowly in the induction period before displaying a sharp increase after $t \approx 300$ ms during the main crystallization process. The increase slows down after $t \approx 1$ s and saturates after $t \approx 10$ s. The averaged crystal size shows a qualitatively similar time trace. The resulting crystallite density first increases slowly. At 100 ms $< t <$ 200 ms there is a small but significant drop,

before the number density displays its fastest increase. This drop can be explained with the competition between growing overcritical and subcritical nuclei [41]. The nucleated crystals grow fast at the expense of the subcritical ones, which are dissolved. After 10 s the number of crystal stays constant.

The crystallization kinetics monitored close to the container wall displays a different kinetics (see figure 5(b)). We detect two types of crystals: wall-oriented crystals of large size and crystals of small size (both can also be identified by eye).

The crystallinity of the large oriented crystals is continuously increasing in the time window of the experiment while the strongest increase is also observed within the first second. The crystal size significantly grows during the same time interval and displays a faster growth velocity than the small randomly oriented crystals (a factor of 10). The larger crystals can be identified at slightly later times compared to the small ones. We determine an approximately constant increasing crystallite density of large crystals.

The fraction of small crystals displays an interesting, quite different behavior. Here the crystallinity first shows a significant decrease before it starts growing. Also the crystal size first decreases before crystal growth takes place after $t \approx 400$ ms. No further growth is detected after $t = 2$ s. The resulting crystal number density is increasing significantly directly after cessation of shear, saturates during the main crystallization (strongest increase in X) and decreases afterward to a plateau.

We suggest that the observations made in the first few hundred milliseconds may be caused by relaxation of the shear-ordered fluid since the shear stress is strongest close to the cell wall, while the shear-ordered fluid at the wall is nucleating on it building shear-and wall-oriented crystals [37, 38]. Shear-ordered regions in a certain distance to the wall decay building smaller and stable crystallites of random orientation which causes the anomalous behavior in the crystallization kinetics of small crystals close to the wall.

At later times ($t > 100$ s) a polycrystal to wall crystal conversion can be identified. Here the amount of wall crystal is increasing, while the amount of polycrystal decreases. At the end of the experiment the observed sample volume is filled with half wall crystals and half polycrystals.

4.2. Time-resolved USAXS data

To get more information about the competition between homogeneous and heterogeneous crystallization thinner sample cells have been used, reducing the amount of homogeneous nucleated crystals. For such experiments an alternative measurement technique has to be used which allows a full sample averaging by detection of the whole Debye–Scherrer cone giving meaningful data investigating small sample volumes. For this purpose additional experiments were performed using silica particles and time-resolved USAXS measurements. Results are shown in figure 6.

The main crystallization process of homogeneous nucleated random oriented crystals is observed till $t = 2.5$ s. Here the crystallinity, the crystal size and the crystal number density display similar time traces: there is a strong increase directly at the beginning of the measurement and saturation at the end of the main crystallization process. The observed behavior is in good agreement with the observation made in the light scattering experiment. In the same time interval the signal obtained from the wall crystal shows a quite different behavior. First the crystallinity stays nearly constant, while the averaged crystal size is decreasing which may be induced by the relaxation of the shear-ordered fluid as discussed above. The start of the main crystallization process is delayed which begins after $t = 1$ s and ends at $t = 2.5$ s like the one of the homogeneous nucleated crystals. Here the crystal size displays its fastest increase, while the number of crystals stays constant: The crystals nucleate during shear relaxation on the wall and grow afterwards while no new crystals appear. The crystal growth velocity of oriented wall crystals is, by a factor of four, larger than the one observed in the polycrystal.

After the main crystallization the measured dataset displays an interesting scenario. In the time interval between 2.5 and 6 s the amounts of wall crystal increases quite fast while the amount of polycrystal decreases. This process

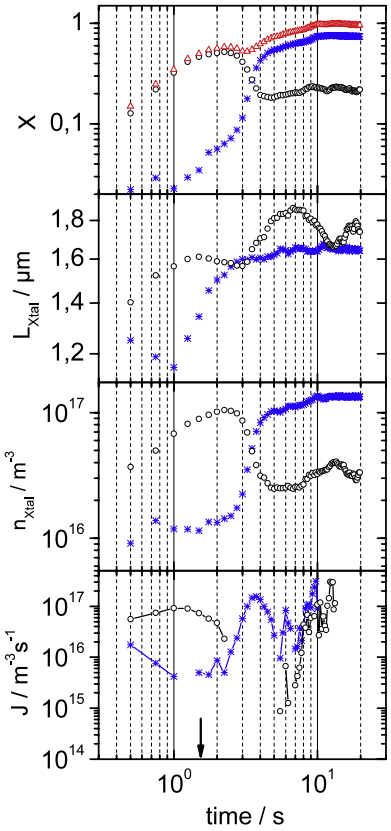

Figure 6. Time traces of the crystallinity X, the average crystal size L_{xtal}, the crystallite number density n_{xtal} and the nucleation rate density J of the Si86 system at $n = 71\ \mu\mathrm{m}^{-3}$ and $c_{\mathrm{NaOH}} = 1.5$ mmol l^{-1} ($\Delta\mu = 0.85 k_{\mathrm{B}}T$) very close to the fluid–solid phase transition determined via USAXS. The black open circles show the results for homogeneous and the blue colored stars for heterogeneous nucleation. The red open squares plot denotes the overall crystallinity in the observed sample volume. The nucleation rate density is given by a three-point smoothing. The arrow represents the time where the sixfold pattern can be first identified.

starts when the total amount of crystals is about 70%. The total number of randomly oriented crystal is decreasing while many new wall-oriented crystals appear. The crystallinity rises slowly to ∼80%. Interestingly the averaged size of the polycrystals is increasing, while the averaged size of the wall crystals stays nearly constant.

These observations may be caused by two effects. Many polycrystals are converted to wall-oriented crystals while crystal ripening in the polycrystal takes place. The latter may be induced by the increasing free volume during the polycrystal to wall crystal conversion. As the averaged crystal size of the wall crystals is only increasing slowly the existing wall crystal is not simply growing at the expense of the polycrystal. Rather the polycrystal is converted into a wall-oriented polycrystalline material. We denote this scenario as a polycrystal to wall crystal conversion process.

At later times (7 s $> t >$ 10 s) a delayed nucleation of polycrystals in the remaining fluid is observed. The averaged size of random oriented crystals is decreasing again, while the crystallinity is slightly increasing. After that 'normal' crystal ripening takes place.

4.3. Nucleation barrier heights

In the framework of classical nucleation theory the nucleation rate density J depends on a kinetic prefactor J_0 as a measure for the number of nucleation sites and on the free energy barrier for nucleus formation ΔG^*: $J = J_0 \exp(-\Delta G^*/k_B T)$. The barrier $\Delta G^* = (16\pi/3)\gamma^3(n\Delta\mu)^{-2}$ is determined by the surface tension γ between the metastable parent phase and the crystal phase and the chemical potential difference between the two phases $\Delta\mu$. The critical size of the nuclei is given by $r^* = 2\gamma/n\Delta\mu$. Analyzing the presented data we are not able to extract either absolute nucleation barrier heights or prefactors. But by identifying the minimal observed crystal size as a measure for the critical nucleus we can give an estimate of the reduction of the nucleation barrier height in the case of heterogeneous nucleation at the container walls. The ratio of the nucleation barrier heights R is proportional to the cube of the ratio of the critical radii: $R = \Delta G^*_{\mathrm{hom}}/\Delta G^*_{\mathrm{het}} = (r^*_{\mathrm{hom}}/r^*_{\mathrm{het}})^3$. For the main crystallization process we obtain $R = 2$ for the data presented in figure 5 and $R = 1.8$ for the data presented in figure 6, showing that the nucleation barrier height is lowered by about a factor of two. Comparing the absolute nucleation rate densities the values for heterogeneous nucleated crystals are below the ones for homogeneous nucleation, which can be explained by a lower kinetic prefactor for heterogeneous nucleation, $J_{0\mathrm{het}} < J_{0\mathrm{hom}}$. The kinetic prefactor on the other side mainly depends on the number of possible nucleation sites and the diffusion of particles to these nucleation sites [14]. The number of nucleation sites for heterogeneous nucleation in our measurements is clearly reduced in comparison to the bulk nucleation due to the restriction of heterogeneous nucleation events to the cell walls and therefore also the diffusion of particles towards the nucleation sites can occur only from a single direction which further reduces the kinetic prefactor.

5. Conclusion

The performed experiments demonstrate the complexity of the crystallization process close to container walls. The competition between the homogeneous nucleated randomly oriented polycrystal and the heterogeneous nucleated oriented wall crystal determines the observed scenario and the arising microstructure. Surprisingly the homogeneous nucleated crystals do crystallize first while the crystallization of the wall crystal is delayed. Nevertheless at the end of the experiment the sample volume close to the wall is either filled with 50% or 80% wall-oriented crystals. When the amount of wall crystal shows its fastest increase the amount of polycrystalline material decreases: the randomly oriented polycrystal is converted into wall crystal. Crystal growth of oriented crystals is favored leading to a large amount of wall-oriented crystal although its nucleation and growth is delayed and its nucleation rate density is surprisingly slightly smaller compared to homogeneous nucleation. The latter observation may be connected with the high undercooling of the melt in the performed experiments.

We presented the first measurements using time-resolved scattering techniques and further data analysis allowing the quantitative description of the competition between heterogeneous and homogeneous nucleation close to a flat wall. Further work is still in progress.

Acknowledgments

We are pleased to thank T Palberg for helpful discussions. Financial support by the DFG (SPP1296 (Pa459/15-1, He1601/23 and He1601/24) and SFB TR6 D1) is gratefully acknowledged.

References

[1] Auer S and Frenkel D 2004 *J. Chem. Phys.* **120** 3015
[2] Cheng Z D *et al* 2002 *Phys. Rev. Lett.* **88** 015501
[3] Dixit N M and Zukoski C F 2001 *Phys. Rev.* E **64** 041604
[4] Ackerson B J and Schätzel K 1995 *Phys. Rev.* E **52** 6448
[5] He Y *et al* 1996 *Phys. Rev.* E **54** 5286
[6] Harland J L *et al* 1995 *Phys. Rev. Lett.* **75** 3572
[7] Schöpe H J, Bryant G and van Megen W 2007 *J. Chem. Phys.* **127** 084505
[8] Gasser U *et al* 2001 *Science* **292** 258
[9] Yethiraj A 2007 *Soft Matter* **3** 1099
[10] Aastuen D J W, Clark N A, Swindal J C and Muzny C D 1990 *Phase Transit.* **21** 139
[11] Ishikawa M and Okubo T 2001 *J. Cryst. Growth* **233** 408
[12] Schöpe H J and Palberg T 2002 *J. Phys.: Condens. Matter* **14** 11573
[13] Wette P, Schöpe H J, Liu J and Palberg T 2003 *Europhys. Lett.* **64** 124
[14] Wette P and Schöpe H J 2007 *Phys. Rev.* E **75** 051405
[15] Cacciuto A and Frenkel D 2005 *Phys. Rev.* E **72** 041604
[16] Hoogenboom J P, Yethiraj A, van Langen-Suurling A K, Romijn J and van Blaaderen A 2002 *Phys. Rev. Lett.* **89** 256104
[17] van Teeffelen S, Likos C N and Löwen H 2008 *Phys. Rev. Lett.* **100** 108302
[18] Rammsteiner I *et al* 2009 *Phys. Rev.* E **79** 011403

[19] Heymann A, Stipp A, Sinn C and Palberg T 1998 *J. Colloid Interface Sci.* **207** 119
[20] Ackerson B J and Clark N A 1981 *Phys. Rev. Lett.* **46** 123
[21] Liu J, Schöpe H J and Palberg T 2002 *J. Chem. Phys.* **116** 5901
[22] de Villeneuve V W A, Verboekend D, Dullens R P A, Arts D G A L, Kegel W K and Lekkerkerker H N W 2005 *J. Phys.: Condens. Matter* **17** 3371
[23] Cacciuto A, Auer S and Frenkel D 2004 *Nature* **428** 404
[24] Stipp A, Biehl R, Preis T, Liu J, Fontecha A B, Schöpe H J and Palberg T 2004 *J. Phys.: Condens. Matter* **16** 3885
[25] Wette P, Schöpe H J and Palberg T 2005 *J. Chem. Phys.* **123** 174902
[26] Dhont J H G, Smits C and Lekkerkerker H N W 1992 *J. Colloid Interface Sci.* **152** 386
[27] Francis P S, Martin S, Bryant G, van Megen W and Wilksch P A 2002 *Rev. Sci. Instrum.* **73** 3878
[28] Wette P, Schöpe H J and Palberg T 2002 *J. Chem. Phys.* **116** 10981
[29] Wette P, Schöpe H J, Biehl R and Palberg T 2001 *J. Chem. Phys.* **114** 7556
[30] Yamanaka J, Hayashi Y, Ise N and Yamaguchi T 1997 *Phys. Rev.* E **55** 3028
[31] Würth M, Culis F, Schwarz J, König P, Palberg T and Leiderer P 1995 *Phys. Rev.* E **52** 6415
[32] Schöpe H J and Palberg T 2001 *J. Colloid Interface Sci.* **234** 149
[33] Roth S V *et al* 2006 *Rev. Sci. Instrum.* **77** 085106
[34] http://pilatus.web.psi.ch/pilatus.html
[35] Stribeck N 2007 *X-ray Scattering of Soft Matter* (Berlin: Springer)
[36] Dux C and Versmold H 1997 *Physica* A **235** 75
[37] Schöpe H J, Decker T and Palberg T 1998 *J. Chem. Phys.* **109** 10068
[38] Ackerson B J and Clark N A 1983 *Physica* A **118** 221
[39] Harland J L and van Megen W 1997 *Phys. Rev.* E **55** 3054
[40] Schöpe H J, Bryant G and van Megen W 2006 *Phys. Rev. Lett.* **96** 175701
[41] Iacopini S, Palberg T and Schöpe H J 2009 *J. Chem. Phys.* **130** 084502